hydrology

MDPI

Article

Evaluating the Combined Impacts of Anthropogenic Disturbances and Climate Change on Future Streamflow Variations in the Minjiang River Basin

Minghao Chen [1,2,*], Kaijie Chen [1,2], Taihua Wang [3] and Cong Li [3]

[1] PowerChina Huadong Engineering Corporation Limited, Hangzhou 311122, China; chen_kj@hdec.com
[2] PowerChina Chongqing Engineering Corporation Limited, Chongqing 401120, China
[3] State Key Laboratory of Hydroscience and Engineering, Department of Hydraulic Engineering, Tsinghua University, Beijing 100084, China; wangtaihua@mail.tsinghua.edu.cn (T.W.); c-li25@mails.tsinghua.edu.cn (C.L.)
* Correspondence: chen_mh4@hdec.com

Abstract

Future streamflow projections are critical for water management. In this study, we coupled the Geomorphology-Based Ecohydrological Model (GBEHM) with the Physics-aware Hybrid Learning and eXtreme Gradient Boosting models to provide a preliminary assessment of streamflow variations in the Minjiang River basin (MRB) over the period of 2020–2099 under the emission scenarios of five CMIP6 models, using data from the 2010s as the baseline. We considered both climatic and anthropogenic influences, assuming that the current anthropogenic disturbances and river network configuration will remain unchanged. The performance of the GBEHM is acceptable, with error metrics exceeding 0.80 and 0.60 before and after the impoundment of the Zipingpu Reservoir, respectively. The cascade of data-driven models demonstrates good performance, with error metrics exceeding 0.90 over the whole simulation period. Under the influence of climate change, the decadal mean streamflow at Zipingpu station will decrease by 2.73–12.16% before 2069 and increase thereafter, while at Gaochang station, it will generally increase by 1.44–13.67% after 2020. Moreover, the decadal mean streamflow at Pengshan station will increase by 13.22–36.41% over the coming decades. However, the combined effects of anthropogenic disturbances and climate change will significantly decrease future streamflow by 61.91–112.16 m^3/s on average, corresponding to a reduction of 14.08–25.51% from the baseline. We also suggest strategies to mitigate future water risks and enhance basin management in the MRB.

Keywords: Minjiang River basin; emission scenario; streamflow

Check for updates

Academic Editors: Yanfang Sang and Tommaso Caloiero

Received: 14 July 2026
Revised: 28 August 2026
Accepted: 8 September 2026
Published: 12 September 2026

Copyright: © 2026 by the authors. Licensee MDPI, Basel, Switzerland. This article is an open access article distributed under the terms and conditions of the Creative Commons Attribution (CC BY) license.

1. Introduction

Rising global temperatures amplify extreme precipitation and, consequently, the frequency of extreme floods [1–4]. These variations will increasingly challenge flood mitigation and water resource management by altering river flow regimes [2,5,6]. Although dams are designed to attenuate flood peaks, anthropogenic disturbances—specifically damming and urbanization—can profoundly modify downstream hydrology, sometimes offsetting or even reversing the intended benefits [4,5].

The Minjiang River basin (MRB) is an important tributary of the upper reaches of the Yangtze River. The Chengdu metropolitan area—a core of the Chengdu–Chongqing Economic Circle—lies within the MRB. The Zipingpu Reservoir (ZR), one of the largest

on the Minjiang River, controls a drainage area of 22,662 km^2 above the dam site, which accounts for 98% of the upper Minjiang River basin, and is located at the outlet of the upstream MRB [7–9]. In the past few decades, streamflow has shown a pronounced decreasing trend in both the upper and lower reaches of the MRB, driven by the combined effects of climate change and anthropogenic disturbances [10–12]. These anthropogenic disturbances include rapid urbanization in the Chengdu metropolitan area, the operation of the ZR, and irrigation in the middle reaches of the MRB. Given the development of the Chengdu metropolitan area and continuous global warming, anthropogenic disturbances and climate change will exert a strong influence on future streamflow variations in the MRB.

Existing studies that adopt multiple approaches have generally indicated that the MRB's streamflow will show significant variations in the future. As an important tributary of the upper reaches of the Yangtze River, the Minjiang River will experience a decrease in its mean annual runoff, consistent with that of the upper Yangtze River, from 2021 to 2070 [13]. By 2100, under SSP5-8.5, blue water in the MRB is projected to decline by 4.4% despite a 6.5% increase in precipitation, driven by a 6.7 °C temperature rise and 13.0% green water growth from 2015 to 2100 [14]. Across four emission scenarios, when the impacts of future climate change and land use change are both considered, the overall trend indicates a decrease in future runoff changes in the MRB from 2015 to 2100 [15]. The runoff in the upper reaches of the Minjiang River exhibits a unique response to climate change; the annual runoff shows an upward trend with increased emissions [16]. However, existing studies have also highlighted significant uncertainties in future streamflow variations [13–16]. Meanwhile, the frequency of flood events will change consistently as well. Design floods at all major hydrological stations in the upper reaches of the Yangtze River are projected to increase in magnitude in the future, while the most extreme historical events are expected to become the new normal [13].

While existing studies have projected streamflow variations under climate change from the 2010s through the 2090s, the overall understanding from these projections could be further strengthened. Specifically, substantial anthropogenic disturbances in the MRB, including the operation of the ZR, the urbanization of the Chengdu metropolitan area, land use change, and agricultural water use, exert a pronounced influence on streamflow variations [10–12,17–19]. However, a comprehensive assessment of this influence remains lacking in previous studies. Moreover, although future streamflow variations in the MRB are reasonably well understood from existing research, the spatial variability of streamflow responses across each reach of the MRB remains poorly understood. Meanwhile, understanding how current land use, reservoir operations, and urban and agricultural expansion influence future streamflow variations in the Chengdu metropolitan area is critical for sustainable water resource management in the region. Overall, comprehensive evaluations of future streamflow variations under current river network configurations and anthropogenic disturbances across the upper, middle, and lower reaches of the MRB are important for future water resource management.

In this study, we assessed future streamflow variations in the upper, middle, and lower reaches of the MRB under the combined impacts of climate change and anthropogenic disturbances. A distributed hydrological model, namely the Geomorphology-Based Ecohydrological Model (GBEHM), was used to capture the runoff generation mechanisms in the MRB. The GBEHM is a physically based, distributed ecohydrological model developed to simulate coupled water, energy, and vegetation processes in river basins with complex terrain [20,21]. Furthermore, a cascade of data-driven models was employed to reproduce the river network routing of runoff to the basin outlet, leveraging their strength in representing complex anthropogenic signals, including reservoir regulation, urban and agricultural water use, and land use change. We used a cascade modeling approach cou-

pling the Physics-aware Hybrid Learning (PaHL) model and the Extreme Gradient Boosting (XGBoost) model to present anthropogenic impacts on streamflow variations in the middle reaches of the MRB. Overall, we (1) employed coupled hydrological–hydrodynamic simulations on streamflow variations in the MRB; (2) assessed the climatic impacts on streamflow variations; and (3) evaluated the combined anthropogenic and climatic impacts on future streamflow variations in the middle reaches of the MRB. Our study contributes to the comprehensive evaluation of climatic and anthropogenic impacts on future streamflow variations in the MRB.

2. Study Area and Data

2.1. Study Area

The MRB (27°49–33°09′ N, 102°32′–105°30′ E) is located in the upper reaches of the Yangtze River, as shown in Figure 1. The MRB covers an area of approximately 135,000 km^2, with the mainstream of the Minjiang River spanning around 735 km, and the Daduhe River is the main tributary [13–15,22]. The Minjiang River is divided into three hydrological reaches: the upper reaches above Dujiangyan, the middle reaches from Dujiangyan to Leshan, and the lower reaches from Leshan to its confluence with the Yangtze River at Yibin. The upper reaches of the MRB are mostly mountainous, while the middle and lower reaches are mostly plains. Most areas of the MRB belong to the subtropical monsoon climate zone with abundant rainfall. The mean annual precipitation is about 800 mm–1200 mm, whilst the mean annual temperature is around 11.03 °C [13–15,22]. The landscape is dominated by forest and grassland, although areas of urban and industrial land use have been steadily increasing in recent years [13–15]. The soil properties in the MRB vary markedly with elevation [18,19]. The soil texture is generally coarse, with silt loam as the dominant fraction.

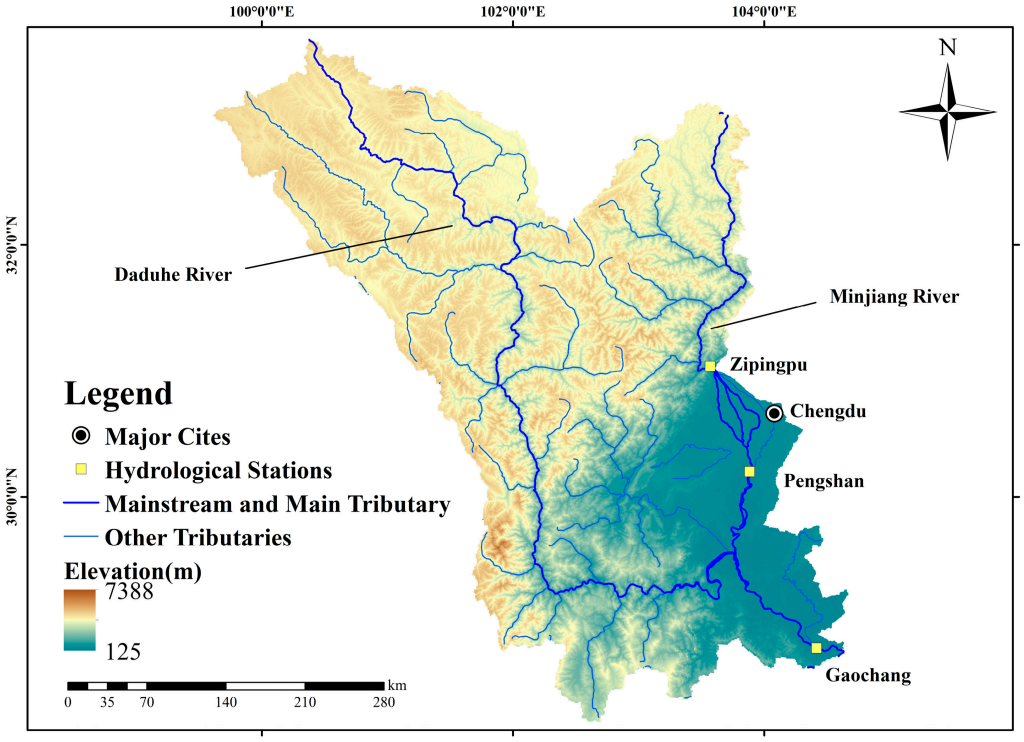


Figure 1. Location, river network and topography of the Minjiang River basin.

The hydrological stations Zipingpu, Pengshan, and Gaochang, which are located near the outlets of the upper, middle, and lower reaches of the MRB, respectively, monitor streamflow variations in the corresponding reaches. The Zipingpu Reservoir, one of the

largest reservoirs on the Minjiang River, is located upstream of the Zipingpu station and reached its full impoundment in 2006. The Zipingpu Reservoir, with a total storage capacity of 1.112×10^9 m^3, was constructed to serve three primary purposes: flood mitigation, hydroelectric power generation, and agricultural irrigation [23]. The Zipingpu Reservoir controls a drainage area of 22,662 km^2 above the dam site, accounting for 98% of the upper MRB [23]. This reservoir also regulates approximately 90% of the flood flows generated by rainstorms in the upper Minjiang River. Pengshan and Gaochang stations monitor streamflow at the outlets of the middle and lower reaches of the MRB, respectively. These two stations control drainage areas of 30,661 km^2 and 135,378 km^2, respectively. The Chengdu metropolitan area is geographically located in the middle reaches of the MRB.

2.2. Data

As illustrated in Table 1, the datasets for the GBEHM employed in this study can be broadly classified into two groups: meteorological forcing data to drive the GBEHM simulations, and underlying-surface data for model parameterization.

Table 1. Basic information on the GBEHM datasets.

ID	Data Group	Data Type	Data Resource
1	Meteorological data	Near-surface meteorological variables	China Meteorological Administration (CMA) Surface Climate Daily Dataset
2		Daily precipitation	China Gauge-based Daily Precipitation Analysis (CGDPA) dataset
3	Underlying-surface data	Topography	Shuttle Radar Topography Mission (SRTM) Digital elevation model
4		Vegetation	GIMMS LAI4g and FPAR4g remote-sensing products
5		Soil texture	Harmonized World Soil Database (HWSD)
6		Soil hydraulic parameters	China Dataset of Soil Hydraulic Parameters
7		Land use	Data Center for Resources and Environmental Sciences, Chinese Academy of Sciences

Meteorological forcing data included daily observations of near-surface meteorological variables, which were obtained from the China Meteorological Administration (CMA) Surface Climate Daily Dataset v3.0 (http://data.cma.cn, accessed on 13 May 2024). Observations from 49 meteorological stations located within the basin and surrounding areas were spatially interpolated to generate gridded forcing fields using the angular distance weighting method [24]. Daily precipitation was derived from the China Gauge-based Daily Precipitation Analysis (CGDPA) dataset [25]. All meteorological variables were prepared at a daily temporal resolution.

Underlying-surface data included topography, vegetation, soil properties, and land use. Topographic data were provided by the Shuttle Radar Topography Mission (SRTM) digital elevation model, with a spatial resolution of 90 m [26]. Data on vegetation conditions were obtained from the GIMMS LAI4g and FPAR4g remote-sensing products [27]. Soil texture data were extracted from the Harmonized World Soil Database (HWSD) [28]. Soil hydraulic parameters were adopted from the China Dataset of Soil Hydraulic Parameters [29]. Land use data, at a spatial resolution of 100 m, were provided by the Data Center for Resources and Environmental Sciences, Chinese Academy of Sciences (http://www.resdc.cn, accessed on 9 July 2024).

The cascade of PaHL and XGBoost models used daily water level and discharge data from the Zipingpu and Pengshan stations to reproduce daily hydrodynamic processes from

2010 to 2019. The GBEHM was constructed from the daily meteorological forcing data and underlying-surface data, as well as daily discharge at Gaochang station for the period of 1980–1999, as illustrated in Table 2.

Table 2. Basic information of the hydrological stations in the study area.

ID	Station Name	Data Type	Time Scale	Period
1	Zipingpu	Water level and discharge	Daily	1980–1999
2	Pengshan	Water level and discharge	Daily	2010–2019
3	Gaochang	Discharge	Daily	1980–1999

3. Methodology

3.1. Projection Framework of Future Streamflow Variations

In this study, we characterized future streamflow variations based on annual mean discharge. Given the impoundment of the Zipingpu Reservoir in 2006, the 2010s were selected as the baseline period for evaluating future streamflow variations, while the periods spanning 2020–2049, 2050–2079, and 2080–2099 represented the near-term, mid-term, and long-term periods in the projections, respectively. Meanwhile, the GBEHM and the cascade of data-driven models were calibrated using data collected before 2010. The baseline dataset was compiled from GBEHM-simulated streamflow at Zipingpu, Gaochang, and Pengshan stations during the 2010s, presenting streamflow that was free from anthropogenic disturbances.

The GBEHM was employed to project future streamflow variations affected by climate change at Zipingpu, Pengshan, and Gaochang stations, taking the output of the climate models as the input. Furthermore, we coupled the GBEHM and data-driven models to project future streamflow at Pengshan station under both climate change and anthropogenic disturbances. In this coupled simulation, streamflow at Zipingpu station, representing the upstream inflow of the middle reaches of the MRB, was simulated using the GBEHM, which was then used to drive the cascade of PaHL and XGBoost models, taking into account anthropogenic disturbances in the middle reaches of the MRB. Thus, in this coupled hydrological–hydrodynamic framework, the GBEHM reproduced runoff generation in the MRB, whereas the data-driven component captured the effects of river network configuration and anthropogenic disturbances on runoff routing via a data-driven approach. The runoff routing was represented by streamflow at the outlet of each reach across the MRB, while the impact of anthropogenic disturbances on streamflow was represented through parameter-controlled statistical relationships within the data-driven models. To evaluate the impacts of current river network configuration and anthropogenic disturbances on future streamflow variations, both numerical models adopted parameters calibrated based on data collected during the 2010s.

We evaluated future streamflow variations under three emission scenarios derived from the Coupled Model Intercomparison Project Phase 6 (CMIP6). We selected a suite of three distinct scenarios representing future emission trajectories of anthropogenic sources, a key deliverable of the Scenario MIP experiment within CMIP6: SSP1-2.6, SSP2-4.5, and SSP5-8.5 [13,30,31]. These three emission scenarios represent the low-end, medium-of-the-road, and high-end scenarios in the range of future pathways, respectively. To simulate hydrological changes in the future period (2020–2100), we collected meteorological outputs from five CMIP6 models in the historical and future periods, namely BCC-CSM2-MR, MRI-ESM2-0, IPSL-CM6A-LR, CNRM-ESM2-1 and EC-Earth3, as illustrated in Table 3 [30]. According to existing studies, these models have demonstrated relatively strong performance in simulating data for the upper reaches of the Yangtze River [32,33].

Table 3. Information on the five selected climate models.

Model Name	Institution Name	Ensemble-Member Identifier	Spatial Resolution
BCC-CSM2-MR	Beijing Climate Center	r1i1p1f1	1.125° × 1.1215°
MRI-ESM2-0	Meteorological Research Institute of the Japan Meteorological Agency	r1i1p1f1	1.125° × 1.1215°
IPSL-CM6A-LR	L'Institut Pierre-Simon Laplace	r1i1p1f1	2.5° × 1.26°
EC-Earth3	EC-Earth-Consortium	r1i1p1f1	0.7° × 0.7°
CNRM-ESM2-1	Centre National de Recherches Météorologiques/Centre Européen de Recherche et de Formation Avancée en Calcul Scientifique	r1i1p1f2	1.4° × 1.389°

The meteorological forcing data for the hydrological model, including precipitation, temperature, wind speed, relative humidity, surface pressure, solar and longwave radiation, and potential evapotranspiration, were generated from the climate models. When applying bias correction and downscaling of CMIP6 models, we adopted a workflow that strictly followed the sequence of "evaluation-first, then bias correction, and finally spatial disaggregation" to ensure the complete removal of systematic biases prior to spatial downscaling, thereby preventing the interpolation process from propagating model errors into the high-resolution products [34]. The performance of each CMIP6 model was evaluated using a multi-criterion scoring method [35]. Then, the quantile delta mapping method (QDM) was adopted for bias correction of the meteorological outputs from the CMIP6 models [13]. Specifically, the cumulative distribution function (CDF) of historical observations, historical data from CMIP6 models, and future data from CMIP6 models—denoted by F1(X), F2(X), and F3(X), respectively—were calculated at each grid box for each month of the year. Subsequently, to correct the future values obtained from the CMIP6 models (Xsim,fut), their cumulative probability F3(Xsim,futl) was calculated. The corresponding values in historical observations (F_1^{-1}(F3(Xsim,fut))) and historical CMIP6 data (F_2^{-1}(F3(Xsim,fut))) were checked. The bias-corrected future values (Xsim,fut_cor) were then calculated using the following two equations:

$$X_{sim,fut_cor} = F_1^{-1}(F_3(X_{sim,fut})) + (X_{sim,fut} - F_2^{-1}(F_3(X_{sim,fut}))) \quad (1)$$

$$X_{sim,fut_cor} = F_1^{-1}(F_3(X_{sim,fut}))\cdot(X_{sim,fut}/F_2^{-1}(F_3(X_{sim,fut}))) \quad (2)$$

We employed Equation (1) to correct the bias of variables that required consideration of their absolute changes, such as air temperature. For variables that required consideration of their relative changes, such as precipitation and wind speed, Equation (2) was adopted for bias correction. The bias correction was applied at the spatial scale to the CMIP6 model outputs.

Subsequently, we downscaled the CMIP6 model outputs after bias correction. In an earlier study, we developed a statistical downscaling approach to transform the outputs of CMIP5 models into high-resolution hydro-meteorological forcing data [34]. A 3 km gridded daily precipitation dataset was used to interpolate and disaggregate the bias-corrected coarse-resolution (approximately 1–2°) outputs of CMIP6 models to a 3 km grid. The downscaled 3 km climate forcing data were further refined to a 1 km × 1 km grid based on elevation–terrain relationships, and were then used to drive the GBEHM. The framework of future streamflow variation projections is shown in Figure 2.

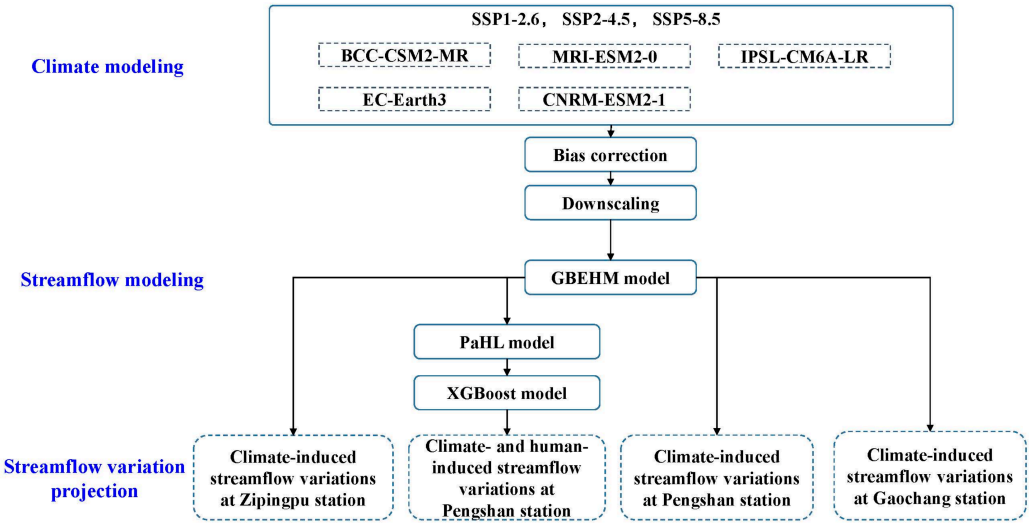


Figure 2. The framework of future streamflow variation projections. Different colors, line styles, and dashed frames are used solely to distinguish the methods from the results and carry no additional meaning.

3.2. Geomorphology-Based Ecohydrological Model

The GBEHM adopts a geomorphology-informed spatial framework, capturing key eco-hydrological feedback while maintaining computational efficiency at the basin scale [35–37]. A multi-layer snow scheme that explicitly resolves mass and energy balance within the snowpack was adopted to simulate snow accumulation and melt, as shown in Equation (3) [38,39]:

$$C_{snow}\frac{\partial T_{snow}}{\partial t} - L_f\frac{\partial \rho_{ice}\theta_{ice}}{\partial t} = \frac{\partial}{\partial z}\left(k_{snow}\frac{\partial T_{snow}}{\partial z}\right) + \frac{\partial I_r}{\partial z} + Q_r \quad (3)$$

where C_{snow} is the volumetric heat capacity of snow; T_{snow} is the snow temperature; t denotes time; L_f is the latent heat of fusion of ice; ρ_{ice} is the density of ice; θ_{ice} is the volumetric ice content; z is the vertical coordinate measured downward from the snow surface; k_{snow} is the thermal conductivity of snow; I_r represents radiative flux penetrating into the snowpack; and Q_r denotes the heat input associated with precipitation.

A fully coupled framework that accounts for conductive heat transfer, advective heat transport associated with water movement, and latent heat exchange during freezing and thawing was used to solve the soil thermal dynamics, as shown in Equation (4) [39,40]:

$$\rho_{ice}\lambda_f\frac{\partial \theta_{ice}}{\partial t} - C_s\frac{\partial T}{\partial t} + \frac{\partial}{\partial z}(k_s\frac{\partial T}{\partial z}) + \rho_{ice}C_{liq}\frac{\partial q_{liq}T}{\partial z} = 0 \quad (4)$$

where T denotes the soil temperature; q_{liq} is the vertical liquid-water flux between soil layers; ρ_{liq} is the density of liquid water; λ_f is the latent heat of fusion for the ice–water phase change; C_s is the bulk volumetric heat capacity of the soil matrix; k_s is the soil thermal conductivity; and C_{liq} is the specific heat capacity of liquid water.

The GBEHM employs the Richards equation to describe vertical water movement in soil. Unsaturated hydraulic conductivity is formulated as a function of unfrozen liquid water content and an ice-impedance factor following the modified Mualem–van Genuchten formulation in Equation (5):

$$K = f_{ice}K_s(\frac{\theta_{liq}-\theta_r}{\theta_s-\theta_r})^{\frac{1}{2}}[1-(1-(\frac{\theta_{liq}-\theta_r}{\theta_s-\theta_r})^{\frac{1}{m}})^m]^2 \quad (5)$$

where K denotes the vertical hydraulic conductivity; K_s is the saturated hydraulic conductivity; θ_{liq} represents the volumetric content of unfrozen liquid water; θ_s and θ_r denote the saturated and residual water content, respectively; m is a dimensionless shape parameter of the soil water retention curve; and the factor f_{ice} is an ice-impedance term that decreases with increasing volumetric ice content, which is commonly specified using empirical relationships [41,42].

Photosynthesis was simulated using the biochemically based Farquhar model, in which canopy assimilation is limited by either Rubisco activity or electron transport, as shown in Equation (6) [43]:

$$A = min(w_c, w_j) \tag{6}$$

where A is the net photosynthetic rate; w_c is the Rubisco-limited carboxylation rate; and w_j is the electron-transport-limited carboxylation rate.

Besides *NSE* and R^2, the percent bias (*PBIAS*) was also used to evaluate the accuracy of the simulation results, as shown in Equation (7):

$$PBIAS = \frac{\sum_{t=1}^{T}(S - M)}{\sum_{t=1}^{T} M} \times 100 \tag{7}$$

where S and M indicate the simulated values and measured values, respectively.

3.3. Constructing the Cascade of Data-Driven Models

In our previous study, we constructed a cascade of data-driven models combining the Physics-aware Hybrid Learning (PaHL) model and the eXtreme Gradient Boosting (XGBoost) model [23]. In this study, we further developed the PaHL model to improve its performance.

To construct the PaHL model, we linearized the hydrodynamic processes by iterating the upstream boundary conditions, rather than using ML algorithms to approximate the full nonlinear dynamics in natural channels [23]. The linear and nonlinear responses of the downstream boundary conditions to the upstream conditions were derived based on the Saint-Venant equations, as follows:

$$\left(Z_{up}^{t}, Z_{down}^{t}, Z_{up}^{t+1}, Q_{up}^{t}, Q_{down}^{t}, Q_{up}^{t+1}, Q_{down}^{t+1}, E\right)\boldsymbol{b_1} = Z_{down}^{t+1} \tag{8}$$

$$\left(Z_{up}^{t}, Z_{down}^{t}, Z_{up}^{t+1}, Z_{down}^{t+1}, Q_{up}^{t}, Q_{down}^{t}, Q_{up}^{t+1}, E\right)\boldsymbol{b_2} = Q_{down}^{t+1} \tag{9}$$

$$Z_c = aZ_{up} + bZ_{down} \tag{10}$$

$$Z_c^{t+1} = Z_c^{t} + ({q_L}^{t} - \frac{({Q_{down}}^{t} - {Q_{up}}^{t})}{\Delta x})\Delta t/t_1 \tag{11}$$

where the superscript and subscript of each variable indicate the time step; $\boldsymbol{b_1}$ and $\boldsymbol{b_2}$ are column vectors composed of coefficients; Z_c indicates the characteristic water level within a channel; Z_{up}, Z_{down}, Q_{up} and Q_{down} are discharge and water level at the upstream and downstream cross sections; q_L indicates the discharge of lateral inflow; and a, b and t1 are parameters to be determined. Equations (8) and (9) and Equations (10) and (11) represent the linear and nonlinear responses, respectively [23]. a and b are the weights of upstream and downstream water levels to the characteristic water level in Equation (11) and are dimensionless. t_1 defines a linear relationship that fits the area of a characteristic cross section as a linear function of the water level Z_c at the cross section, thereby having a dimension of m. a and b range from -10 to 10 and from 0 to 2.0, respectively, while the values of t_1 are estimated after the calibration of a and b. These three parameters were calibrated using the Genetic Algorithm [23].

We iterated the upstream boundary conditions via weighted averaging. The downstream boundary conditions were simulated using the linear and nonlinear relationships, and the error metrics were simultaneously calculated. Then, the upstream conditions and simulated downstream conditions were weighted, with the error metrics used as weights, as follows:

$$U_i = (U_o + \sum_{i=1}^{n} D_s E_i)/(1 + \sum_{i=1}^{n} E_i) \quad (12)$$

where U_i and U_o indicate the iterated and origin upstream boundary conditions, respectively; D_s and E indicate the simulated downstream conditions and error metrics at the downstream cross section, respectively; n denotes the error metrics used for iterations. Assuming that simulation accuracy at the downstream cross section is sufficiently high, the upstream conditions will approximate the downstream conditions with ongoing iterations, thereby increasing the linearity between boundary conditions. We iteratively updated the upstream boundary conditions using linear and nonlinear simulations to obtain the output matrix of corresponding downstream boundary conditions. The output matrix merges the simulation results based on both linear and nonlinear responses.

The PaHL model adopted 21 iterations to augment the output matrix, which was fed into the XGBoost model; in turn, the XGBoost model was trained to map from the output matrix to the observed downstream discharge. The PaHL model was trained using the upstream, downstream, tributary, and lateral inflow data during the calibration period. In the validation and test periods, only the upstream, tributary, and lateral inflow data were used as model inputs, while the downstream observations were reserved for independent performance evaluation. To prevent data leakage, the observed downstream discharge and water level after the calibration period were strictly isolated from the calibration process of the PaHL and XGBoost models.

The XGBoost model is an ensemble learning framework based on gradient-boosted decision trees [44]. It enhances the traditional Gradient Boosting Decision Tree model with regularization, second-order approximation of the loss, column subsampling, and tree complexity control, effectively preventing overfitting and accelerating training. XGBoost supports custom loss functions, handles missing values automatically, and is robust to feature collinearity, making it ideal for structured tabular data and nonlinear regression tasks. Its core objective is illustrated in Equation (13):

$$\mathcal{L}^{(t)} = \sum_{i=1}^{n} l(y_i, \hat{y}_i^{(t-1)} + f_t(x_i)) + \Omega(f_t) \quad (13)$$

The framework of the cascade of data-driven models is shown in Figure 3.

The Nash–Sutcliffe Efficiency (*NSE*), Coefficient of Determination (R^2), and Kling–Gupta Efficiency (*KGE*) were used as the error metrics, as illustrated by Equations (14)–(16).

$$NSE = 1 - \sum_{i=1}^{n} (M_i - S_i)^2 / \sum_{i=1}^{n} (M_i - \overline{M})^2 \quad (14)$$

$$R^2 = (\sum_{i=1}^{n} (M_i - \overline{M})(S_i - \overline{S}) / \sqrt{\sum_{i=1}^{n} (M_i - \overline{M})^2 \sum_{i=1}^{n} (S_i - \overline{S})^2})^2 \quad (15)$$

$$KGE = 1 - \sqrt{(r-1)^2 + (\alpha - 1)^2 + (\beta - 1)^2} \quad (16)$$

where S and M indicate the simulated values and measured values, respectively; $\overline{S}$ and $\overline{M}$ indicate the mean simulated and measured values, respectively; r, α, and β indicate the Pearson correlation coefficient, variability ratio, and bias ratio, respectively. A high R^2 value signifies that the model explains the vast majority of the observed variance, indicating that the simulated hydrograph follows the observed temporal dynamics with strong linear correspondence. A high *NSE* value indicates that the model produces a root-mean-square

error substantially smaller than the variance of the observed series, meaning that the simulation captures the magnitude and timing of peaks with low residual errors. A high *KGE* value suggests that the model maintains a balanced performance across correlation, bias, and variability, reproducing the observed variability with reasonable fidelity.

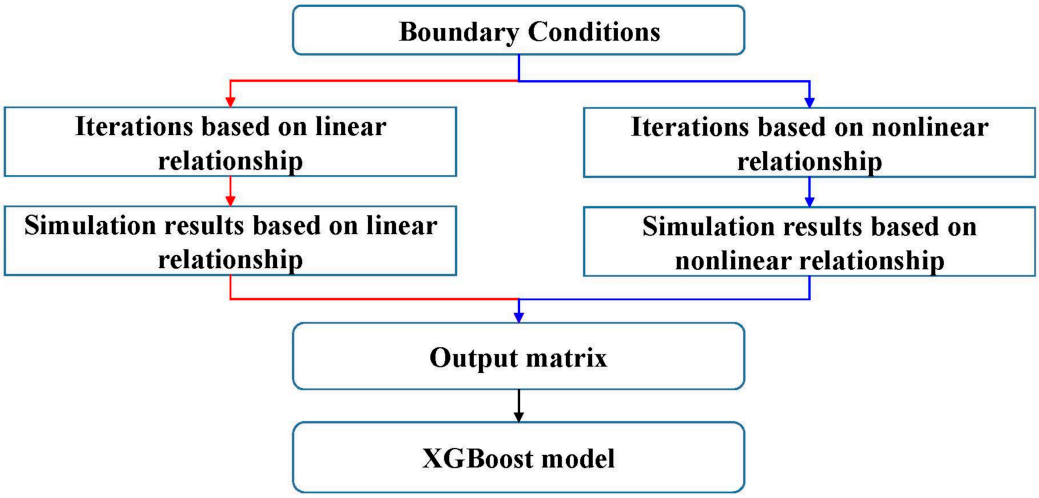


Figure 3. The framework of the cascade of PaHL and XGBoost models.

4. Results

4.1. Performance Evaluation of Numerical Models

We adopted a previously established GBEHM to reproduce the hydrological process in the MRB [10]. According to earlier studies, the Manning coefficients, surface retention capacity, and plant root depth are vital parameters for the performance of the GBEHM [33,35–37]. These parameters were initially derived based on physical considerations and then optimized via a series of parametric experiments to derive the final calibrated values. As a result, the Manning coefficients of hillslope range from 0.1–0.5 $s \cdot m^{-1/3}$; the surface retention capacity ranges from 10 to 30 mm; and the plant root depth varies from 0.1 to 2.0 m. The initial soil temperature profile was estimated based on a linear relationship between ground temperature and elevation. The initial values of the hydrological variables, including soil moisture, soil ice content, ground temperature, and water table depth, were obtained from the corresponding datasets. The GBEHM was calibrated for the period 1980–1992 and validated for the period 1993–1999, and calibrated for the period 2010–2015 and validated for the period 2016–2019, using data collected at Zipingpu and Gaochang stations; the GBEHM was then used to project the streamflow for the period 2020–2099. The GBEHM adopted a 1 km × 1 km grid. The MRB was discretized into 351 sub-basins, with the main channel of each sub-basin defining the runoff routing pathway. Each 1 km × 1 km grid cell was further represented as several topographically similar hillslope–valley systems, with hillslope serving as the fundamental unit for eco-hydrological simulation. The GBEHM employed a physically based parameterization scheme, with parameters related to vegetation type, soil properties, and terrain characteristics. In the GBEHM, we considered the combined effects of reservoirs in the upper reaches of the MRB. As mentioned, land use data during 1980–1999 were used to calibrate the GBEHM for historical streamflow simulations and future streamflow projections.

Historical streamflow data at Zipingpu, Pengshan, and Gaochang stations were used to construct the GBEHM. The error indicators for the simulation results obtained by the GBEHM are summarized in Table 4. In general, the GBEHM adequately represents the dominant runoff generation and routing processes in the MRB. At Zipingpu and Gaochang stations, the *NSE* and R^2 range from 0.81 to 0.89, with the *PBIAS* ranging from −6.25 to

−8.47%. However, the GBEHM shows worse performance at Pengshan station, with *NSE* and R^2 ranging from 0.67 to 0.75. This may indicate the influence of the Zipingpu Reservoir.

Table 4. Performance statistics of daily runoff simulations at Gaochang hydrological station during calibration and validation periods.

Station	Time Period	*NSE*	R^2	*PBIAS* (%)
Zipingpu	Calibration (1980–1992)	0.88	0.89	−8.47
	Validation (1993–1999)	0.83	0.84	−6.85
Pengshan	Calibration (2010–2015)	0.73	0.75	−11.36
	Validation (2016–2019)	0.67	0.69	−18.78
Gaochang	Calibration (1980–1992)	0.87	0.87	−8.13
	Validation (1993–1999)	0.81	0.84	−6.25

We adopted streamflow data during the baseline period (2010–2019) at Pengshan station to train the PaHL and XGBoost models. The water levels and discharge rates at Zipingpu and Pengshan stations, as well as the discharge of tributaries and lateral inflow, were used to construct the PaHL and XGBoost models, with the water levels estimated based on the water level–discharge curve. The cascade of data-driven models used 6 years of data for calibration, 2 years of data for validation, and 2 years of data for testing.

For the PaHL model, the values of the key parameters a and b range from −4.13 to 9.46 and from 0.19 to 1.84, respectively, while the values of t_1 are related to the values of a and b. The XGBoost model was configured with the following hyperparameters: the number of boosting trees was set to 500, the learning rate to 0.03, and the maximum tree depth to 8.0. To further control overfitting, the subsample ratio of training instances and the column subsample ratio of features were both set to 0.9, and L2 regularization was applied with a lambda of 1.0. The objective function adopted the standard squared error loss.

As illustrated in Table 5, the cascade of data-driven models generally achieved good accuracy during the whole simulation period, with the three error metrics exceeding 0.90. In the calibration period, the values of the three error metrics approached 0.98. Nevertheless, the accuracy of the cascade of data-driven models decreased in the validation and test periods, with the values of the three error metrics ranging from 0.68 to 0.91. Given that the correlations between upstream and downstream variables have a notable influence on the performance of the PaHL model, this fluctuation in errors can be attributed to a drift in upstream–downstream correlations. The R^2 values between upstream and downstream discharge varied from 0.53 in the calibration period to 0.14 in the validation period and 0.66 in the test period, as shown in Figure 4. The weak upstream–downstream correlation during the validation period is largely attributable to the operation of the Zipingpu Reservoir not being included in the GBEHM during calibration. Therefore, the PaHL model, which captured the stronger upstream–downstream correlation in the calibration period, could not effectively capture this correlation in the validation period. As a result, the cascade of PaHL and XGBoost models showed worse performance during the validation period. However, despite the influence of upstream–downstream correlation drift, the values of the three error metrics exceeded 0.90 over the whole simulation period. Thus, the cascade of data-driven models can reliably project future streamflow under changing conditions.

Table 5. Performance statistics of daily streamflow simulated by the cascade of data-driven models at Pengshan station during the calibration period, validation period, test period, and whole simulation period (2010–2019).

Simulation Period	*NSE*	R^2	*KGE*
Calibration period (2010–2015)	0.98	0.98	0.97
Validation period (2016–2017)	0.68	0.78	0.72
Test period (2018–2019)	0.85	0.87	0.91
Whole simulation period (2010–2019)	0.96	0.92	0.93

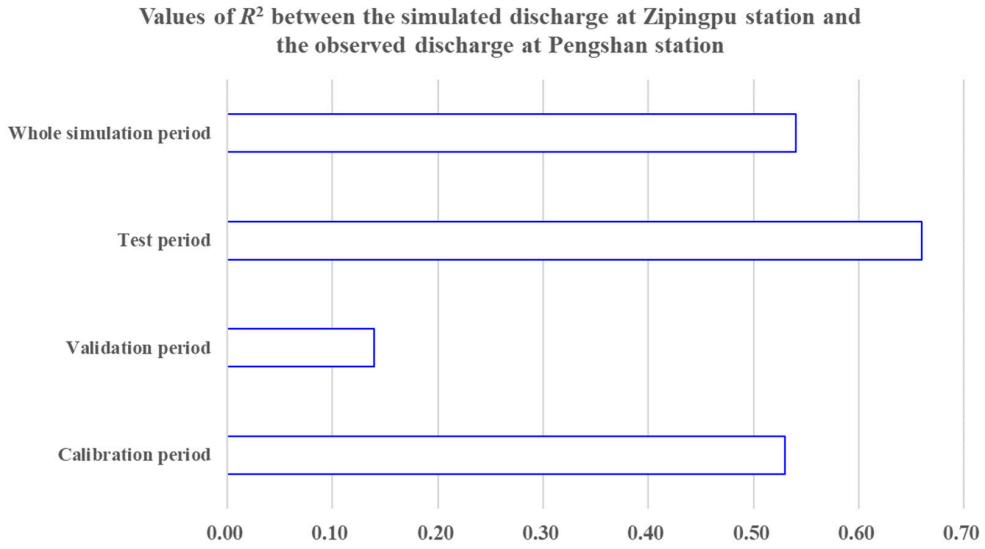


Figure 4. Values of R^2 between simulated discharge at Zipingpu station and observed discharge at Pengshan station across different simulation periods.

As shown in Figure 5, the cascade of data-driven models effectively reproduced the streamflow at Pengshan station with a low discharge over the whole simulation period. The cascade of data-driven models also exhibited good performance in simulating streamflow with a high discharge during the calibration period. While the drift in upstream–downstream correlations weakened the performance of the cascade of data-driven models in the validation period, the fluctuation in streamflow during the test period was generally captured. Overall, the cascade of data-driven models is capable of reproducing daily streamflow variations at Pengshan station.

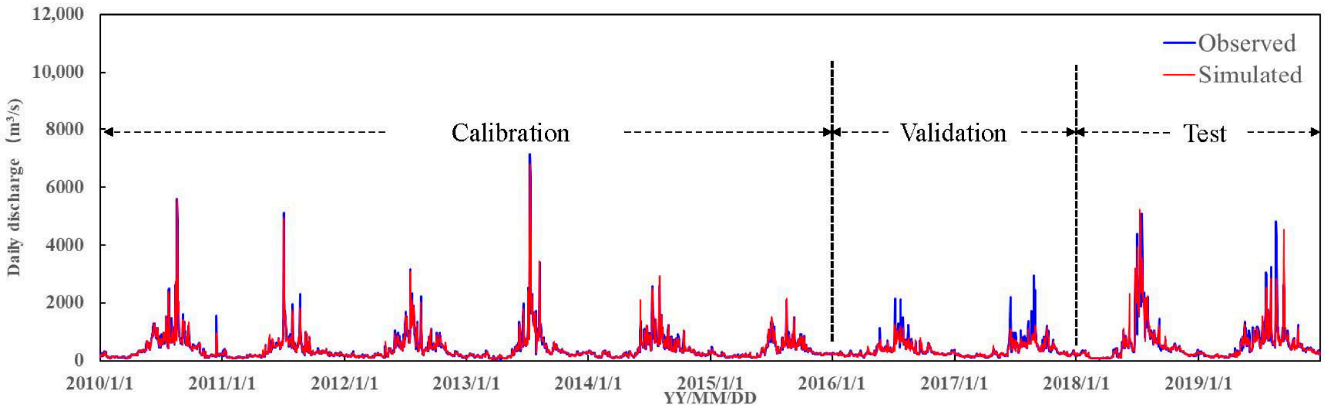


Figure 5. Comparison of observed and simulated daily runoff by the cascade of data-driven models at Pengshan station during the baseline period (2010–2019).

4.2. Streamflow Variations Under Climate Change

Since the streamflow at Zipingpu, Pengshan, and Gaochang stations during the baseline period was simulated using the GBEHM based on the outputs of the CMIP6 models, the difference between projected and baseline streamflow represents climate-induced streamflow variations at the three stations. The results indicate that future annual mean streamflow exhibits a diverse trend in the coming decades.

Violin plots were constructed to show the distribution of projected streamflow values at the three stations under each emission scenario, as shown in Figure 6a–c. The sample size of each violin differs between the baseline and future periods. Specifically, the baseline distribution comprises 10 annual values from 2010 to 2019. Each future decade (2020s–2090s) comprises 50 annual values, that is, 10 years × 5 climate models, thus quantifying the uncertainty arising from the combination of inter-model spread and inter-annual variability under each emission scenario. As shown in Figure 7a–c, for each emission scenario and decade, we calculated the percentages of 50 CMIP6 simulations to obtain the mean decadal discharge values above and below the baseline.

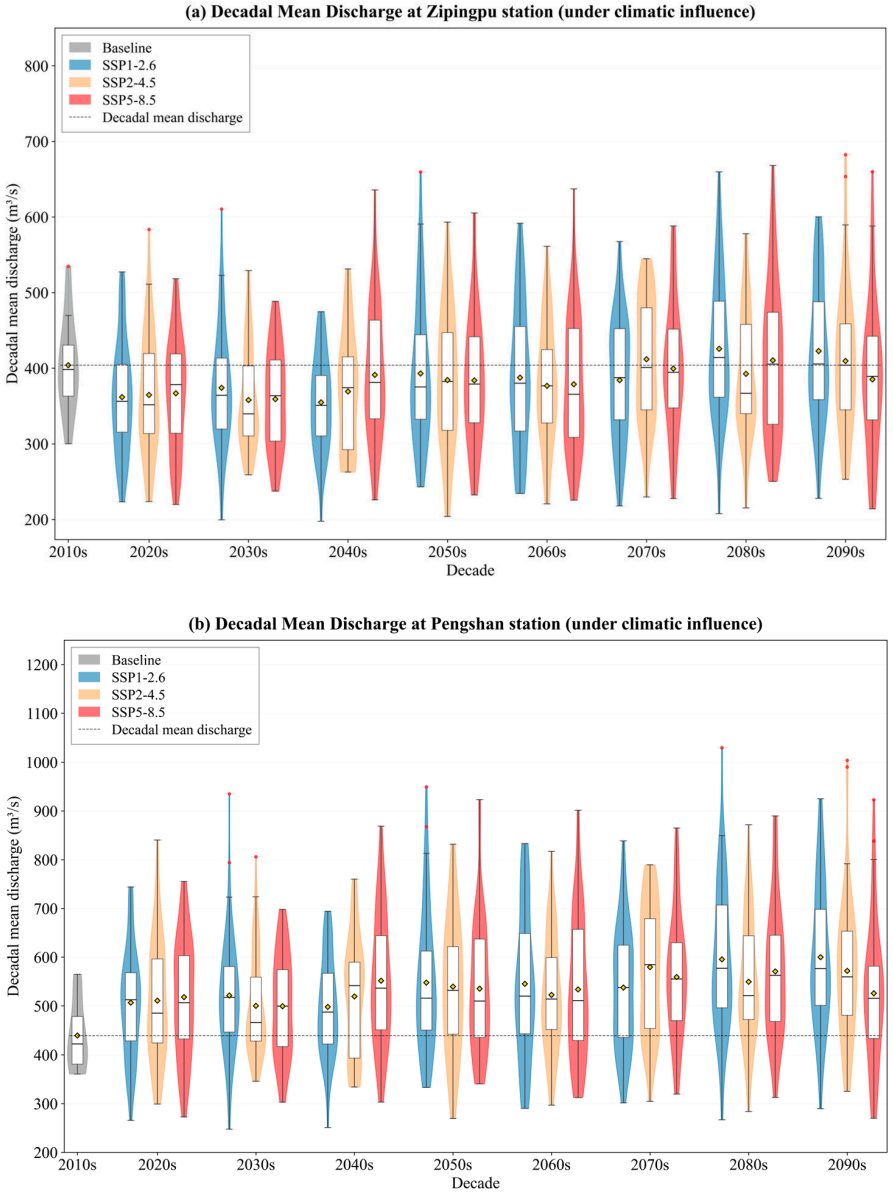


Figure 6. *Cont.*

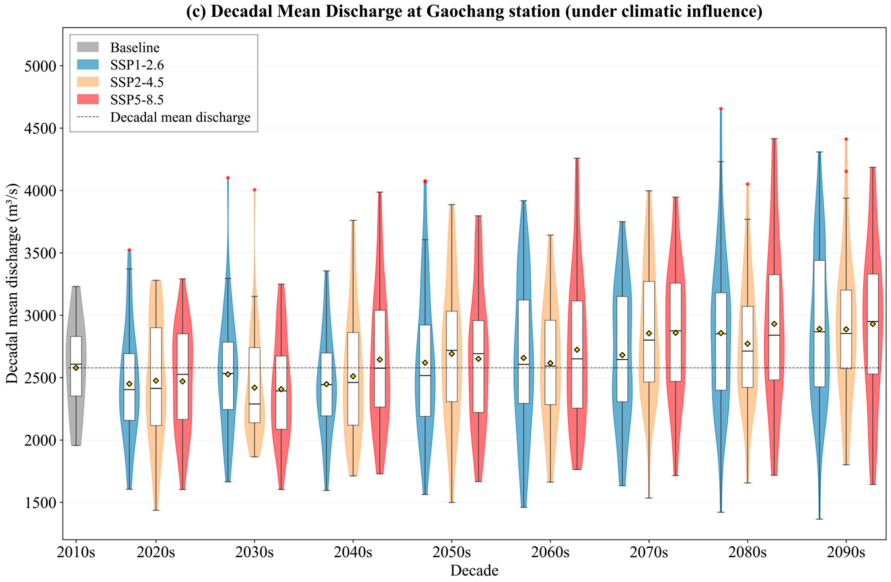


Figure 6. Streamflow variations at Zipingpu (**a**), Pengshan (**b**), and Gaochang (**c**) stations. Each violin represents the distribution of multi-model projections for a given scenario, combining all available model members. In the decadal violin plots, each violin body represents the kernel density estimate of the annual mean flow distribution for a given decade and emission scenario, with the local width proportional to the sample density, thereby revealing the overall distributional shape, including modality and skewness. The overlaid boxplot elements summarize the key statistics: the box spans the interquartile range (IQR, 25th–75th percentiles), with the internal horizontal line denoting the median and the gold diamond representing the arithmetic mean; the whiskers extend to the most extreme data points within 1.5 × IQR, with the outliers beyond this range plotted as red dots.

During the baseline period, the maximum, minimum, and mean daily streamflow at Zipingpu station were 6909.36 m^3/s, 57.31 m^3/s, and 403.97 m^3/s, respectively. At Pengshan station, the corresponding values were 7150.00 m^3/s, 13.00 m^3/s, and 439.71 m^3/s, respectively, while at Gaochang station, they were 25,943.63 m^3/s, 323.81 m^3/s, and 2578.43 m^3/s, respectively.

The projected annual mean streamflow at the three stations generally exhibits an increasing trend from the 2020s to the 2090s under climatic influence. However, compared with the baseline period, the projected decadal mean streamflow varies across stations. At Zipingpu station, the decadal mean discharge declines from 404.00 m^3/s during the 2010s to 354.86–392.98m^3/s (range of multi-model means) in the period 2020–2069 under all three emission scenarios, showing a reduction of 2.73–12.16%. This declining trend is supported by 58–76% of the CMIP6-based projections under each emission scenario. In contrast, the projected streamflow exceeds the baseline level during the 2070s, 2080s, and 2090s across specific emission scenarios, a finding that is supported by more than 50% of the CMIP6-based projections.

The decadal projections of the GBEHM also converge on diverse trends at Pengshan and Gaochang stations. At Pengshan station, the decadal annual mean streamflow after 2020 is projected to exceed the baseline by 58.14–160.09 m^3/s (range of multi-model means) under the three emission scenarios, diverging by 13.22–36.41% from the baseline values. This increasing trend is supported by 62–90% of the CMIP6-based projections under each emission scenario. At Gaochang station, compared with the baseline level, the decadal mean streamflow is projected by the GBEHM to decrease by 51.26–170.85 m^3/s (range of multi-model means) from 2020 to 2049, corresponding to a reduction of 1.99–6.63% from the baseline values. Under each emission scenario, 50–70% of the CMIP6-based projections agree on this decreasing trend. In contrast, the decadal streamflow at Gaochang station is

projected by the GBEHM to exceed the baseline by 37.07–352.38 m^3/s (range of multi-model means) under the three emission scenarios from 2050 to 2099, diverging by 1.44–13.67% from the baseline values. This increasing trend is generally supported by 50–74% of the CMIP6-based projections.

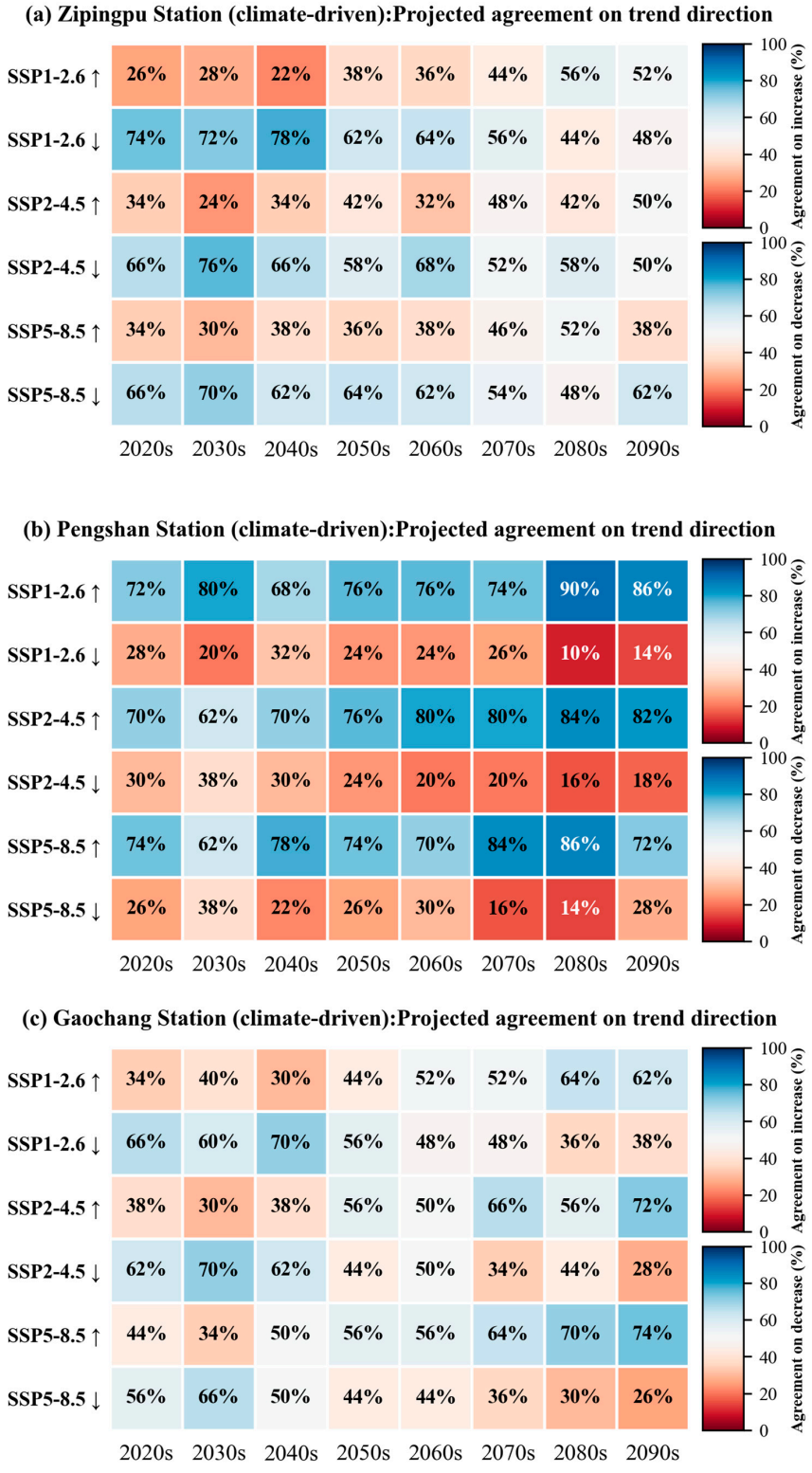


Figure 7. The percentages of the 50 CMIP6 simulations that yielded mean decadal discharges above and below the baseline for each emission scenario and decade at Zipingpu (**a**), Pengshan (**b**), and Gaochang (**c**) stations. Upward and downward arrows indicate increasing and decreasing trends, respectively.

4.3. Combined Anthropogenic and Climatic Impacts on Streamflow Variations

The combined anthropogenic and climatic impacts on streamflow were simulated by coupling the GBEHM with the PaHL and XGBoost models, based on the outputs of the CMIP6 models. The representativeness of training data is vital for the performance of the cascade of data-driven models. Hence, we compared the historical and future ranges of daily streamflow at Zipingpu station, which provides an important boundary condition for the cascade of data-driven models. The historical daily streamflow data were extracted from the baseline. As shown in Figure 8, future daily streamflow at Zipingpu station is projected to mostly fall within the range of historical daily streamflow at this station. In addition, extremely high and low daily streamflow values exceeding the upper and lower bounds account for around 0.33%. Accordingly, the training data adequately represent the range of future boundary conditions. Therefore, the cascade of data-driven models is expected to maintain its predictive performance in future simulations.

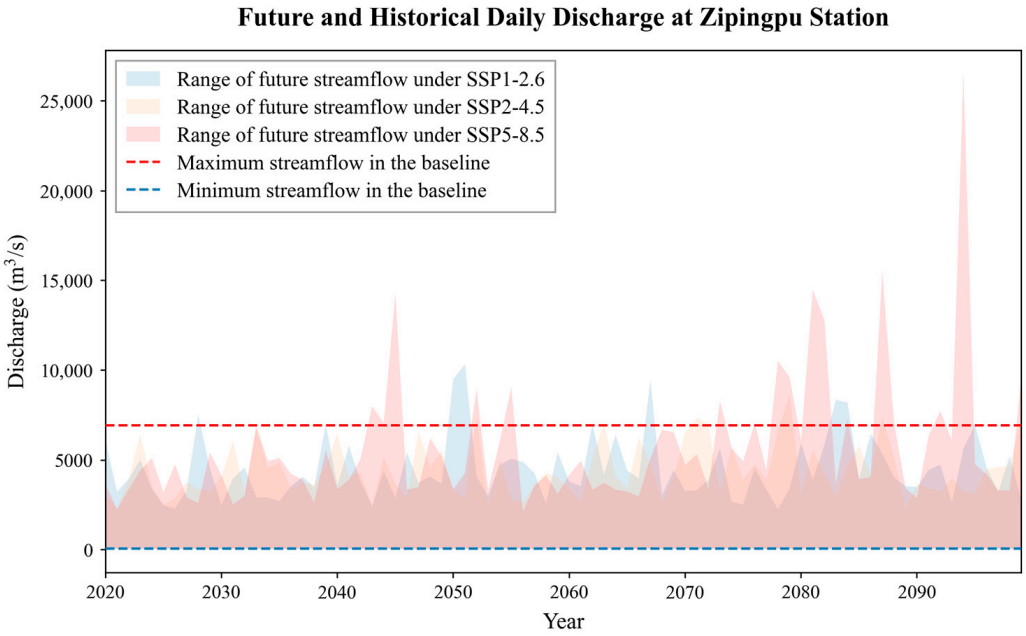


Figure 8. The range of historical and future daily streamflow at Zipingpu station.

Under combined climatic and anthropogenic effects, the annual mean streamflow at Pengshan station declines markedly after 2019. Relative to the baseline, the decadal streamflow is projected to decrease by 61.91–112.16 m^3/s (range of multi-model means) under the three emission scenarios, corresponding to a reduction of 14.08–25.51% from the baseline, as shown in Figure 9. As shown in Figure 10, under the combined effects of anthropogenic disturbances and climate change, the mean decadal streamflow at Pengshan station exhibits a pronounced decreasing trend compared to the baseline across all decades and emission scenarios. However, with multiple extreme hydrological events, the mean decadal streamflow at Pengshan station will exceed the baseline. As shown in Figure 11, 0.00–24.0% of the CMIP6-based projections present this increasing trend under each emission scenario. In contrast, the decreasing trend is more significant before 2050 than after 2050. Overall, under the combined influences of anthropogenic disturbances and climate change, the decadal daily streamflow at Pengshan station is projected to decline consistently and substantially over the coming decades.

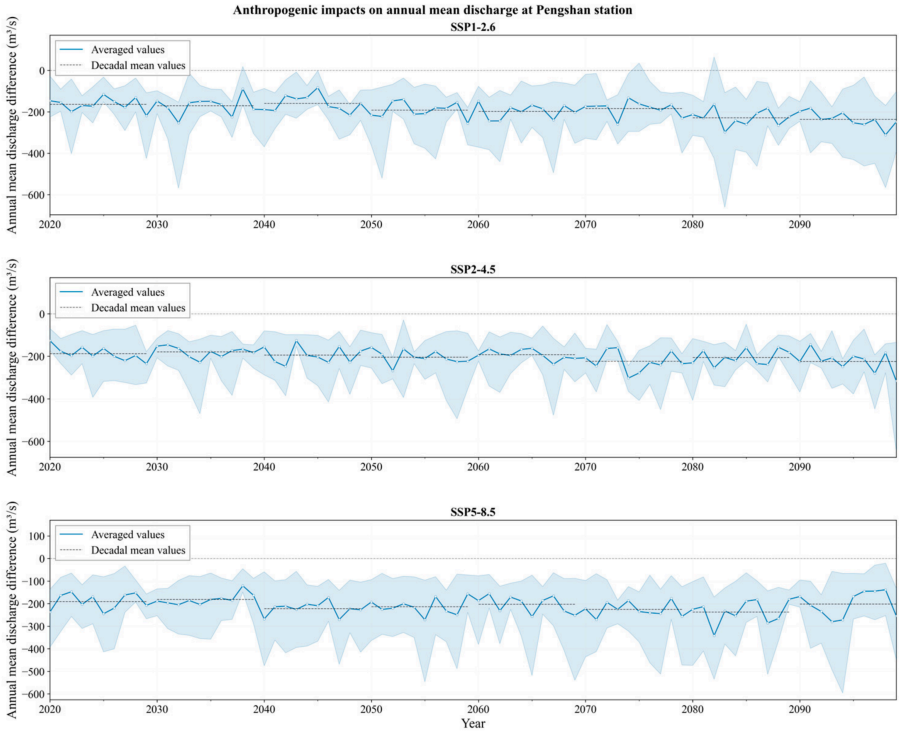


Figure 9. Streamflow variations at Pengshan station caused by anthropogenic disturbances. The shaded area in the figure represents the envelope between the maximum and minimum decadal mean discharge values.

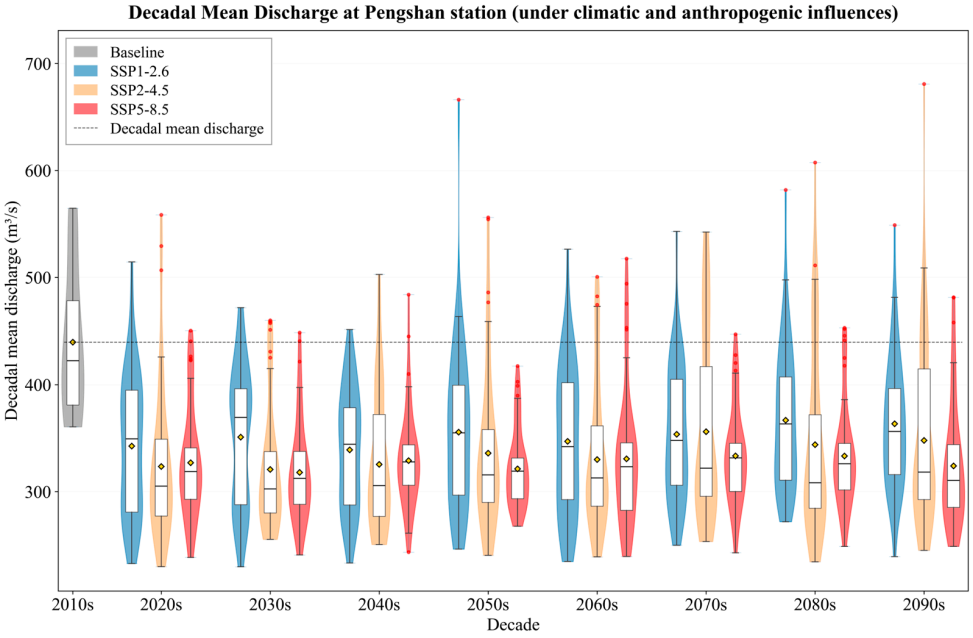


Figure 10. Each violin represents the distribution of multi-model projections for a given scenario, combining all available model members. In the decadal violin plots, each violin body represents the kernel density estimate of the annual mean flow distribution for a given decade and emission scenario, with the local width proportional to the sample density, thereby revealing the overall distributional shape, including modality and skewness. The overlaid boxplot elements summarize the key statistics: the box spans the interquartile range (IQR, 25th–75th percentiles), with the internal horizontal line denoting the median and the gold diamond representing the arithmetic mean; the whiskers extend to the most extreme data points within 1.5 × IQR, with the outliers beyond this range plotted as red dots.

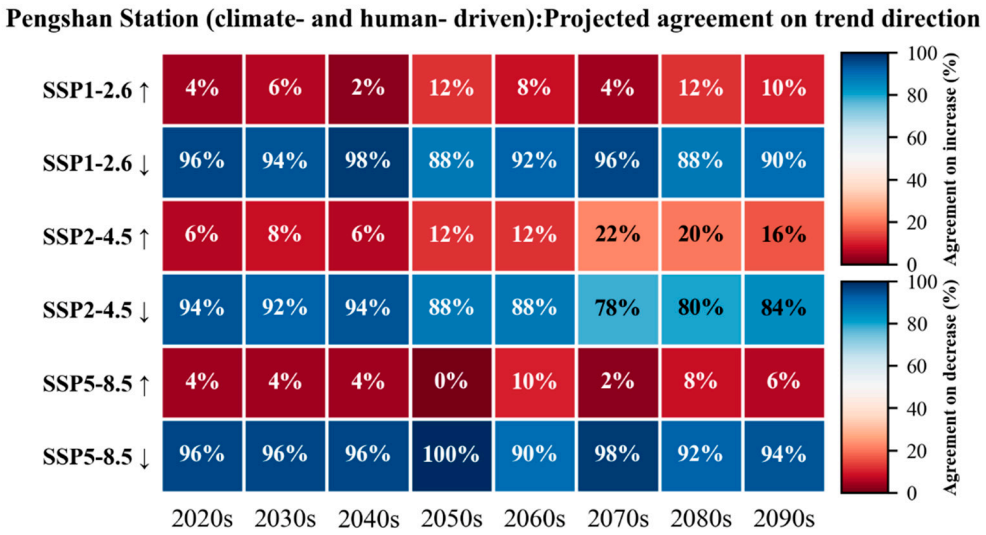


Figure 11. The percentages of the 50 CMIP6 simulations that yielded mean decadal discharges above and below the baseline for each emission scenario and decade at Pengshan station. Upward and downward arrows indicate increasing and decreasing trends, respectively.

5. Discussion

5.1. Climate-Induced Streamflow Variations in the Minjiang River Basin

While existing studies generally projected decreasing trends of annual discharge in the MRB, they also highlighted the notable diversity in future streamflow variations [13–17,19]. Our findings further suggest that changes in future streamflow exhibit variable trends across the upper, middle, and lower reaches of the MRB under the influence of climate change.

At Zipingpu and Gaochang stations, future streamflow is projected to generally decline in the near term, as shown in Figure 6a–c, a finding that is consistent with earlier studies [13–15]. However, it is expected to increase in the long term at Zipingpu station and in both the medium and long terms at Gaochang station. Meanwhile, decadal streamflow variations exhibit more consistent increasing trends at Pengshan station than at the other two stations, as shown in Figure 6a–c. As shown in Figure 7a–c, more CMIP6-based projections (62–90%) support the trend of streamflow variations at Pengshan station than at the other two stations (58–76% and 50–70%, respectively). Thus, the projected future streamflow trends exhibit distinct spatial patterns across the upper, middle, and lower reaches of the MRB. Existing studies have provided limited assessments of future streamflow variations along the three reaches of the MRB; thus, our work helps to fill this gap and enhances the understanding of future streamflow variations in the region [13–17,19].

As hydrological-model parameter uncertainty, GBEHM structural uncertainty, and bias-correction uncertainty have unknown influences on future streamflow variations, we based our calculations on the historical and future simulations of the GBEHM. Hence, the uncertainties associated with the parameterization and structure of the GBEHM may cancel out to some extent when comparing the historical and future periods. Further studies are needed to identify and quantify the uncertainties associated with the parameterization and structure of the GBEHM. It is also valuable to examine whether the urbanization of the Chengdu metropolitan area leads to lower variations in streamflow trends in the middle reaches of the MRB.

5.2. Anthropogenic Impacts on Streamflow Variations in the Middle Reaches of the Minjiang River Basin

Complex river networks, intensive influence from human activities in the Chengdu metropolitan area, and poorly documented operation rules for water conservancy projects

collectively limit our understanding of the anthropogenic impacts on future streamflow in the middle reaches of the MRB [45,46]. In this study, we effectively reproduce daily streamflow variations under the combined influences of climate change and anthropogenic disturbances. Although the drift in upstream–downstream correlations and uncertainties from multiple origins affect the performance of data-driven simulations, our work provides the first assessment of streamflow changes in the data-scarce MRB under the combined effects of complex anthropogenic disturbances and climate change.

As shown in Figures 9–11, the combined anthropogenic and climatic effects decrease the decadal mean streamflow at Pengshan station by 61.91–112.16 m^3/s (range of multi-model means) under the three emission scenarios, diverging by 14.08–25.51% from the baseline. However, the decadal annual mean streamflow after 2020 exceeds the baseline by 58.14–160.09 m^3/s at Pengshan station under the influence of climate change. Accordingly, anthropogenic disturbances have a significant effect on future streamflow at Pengshan station. As shown in Figure 11, 76–100% of the CMIP6-based projections also suggest such anthropogenic effects across all emission scenarios, indicating that these effects exist in multiple future scenarios. This finding suggests that anthropogenic disturbances in the middle reaches of MRB exert a significant influence on streamflow variations in both historical and future periods [43].

The uncertainties in data-driven models derive from the uncertainties in these models' input, parameterization, and structure. Based on our comparison, the training data adequately represent the range of future boundary conditions; that is, the cascade of data-driven models can maintain its predictive performance in future simulations. However, the effects of uncertainties in GBEHM simulations, upstream–downstream correlation drift, and uncertainties in model parameterization and structure are still unclear. A more thorough evaluation of these uncertainties is needed to refine the projections of future streamflow variations.

5.3. Implications of Projected Streamflow Variations for Water Resource Management in the Minjiang River Basin

The diverse trends of future streamflow variations pose challenges to water security in the MRB, a region vital to the development of the Chengdu metropolitan area. Under climate change, the decadal mean streamflow is projected to decrease at Zipingpu station in both the near- and mid-term periods, and to decrease in the near-term period at Gaochang station. The combined effects of climate change and anthropogenic disturbances are projected to significantly influence the decadal mean streamflow at Pengshan station in the coming decades.

Thus, the near- and mid-term water scarcity risks in the upper reaches of the MRB warrant close attention from both policymakers and water managers. Given the high intensity of hydropower development in the upper reaches of the MRB, integrated management of the cascade power stations is essential to enhance streamflow reliability [7–9]. Moreover, considering the pronounced effects of anthropogenic disturbances on future streamflow variations in the middle reaches of the MRB, the coordinated management of water withdrawal, use, consumption, and discharge will help to safeguard effective water supply in this region. Critically, uncertainties in future streamflow variations may lead to drought–pluvial seesaws, calling for the development of resilient management strategies in the MRB [13]. This resilient management framework should combine pre-flood reservoir drawdown, real-time rule curve adjustments, and rapid switching between flood-control and water-supply operations to mitigate the impacts of drought–flood alternation. Overall, a better understanding of future water management pathways can inform proactive adaptation to emerging water challenges.

6. Conclusions

In this study, we coupled the GBEH with the PaHL and XGBoost models to project anthropogenic and climatic impacts on streamflow variations in the MRB under SSP1-2.6, SSP2-4.5, and SSP5-8.5 scenarios. The GBEHM and the cascade of PaHL and XGBoost models exhibit good performance in evaluating future streamflow variations across the different reaches of the MRB.

(1) The error metrics of the GBEHM exceed 0.80 and 0.60 before and after the impoundment of the Zipingpu Reservoir, respectively, indicating acceptable accuracy. Under the influence of upstream–downstream correlation drift, the cascade of PaHL and XGBoost models shows good performance, with error metrics exceeding 0.90 over the whole simulation period.

(2) The decadal mean streamflow at Zipingpu station is projected to decrease by 2.73–12.16% from 2020 to 2069 and increase thereafter, while at Gaochang station, it is projected to increase by 1.44–13.67% from 2020 to 2099. In contrast, the decadal mean streamflow at Pengshan station is expected to increase by 13.22–36.41% in the coming decades.

(3) The combined effects of anthropogenic disturbances and climate change significantly influence future streamflow variations at Pengshan station. The decadal mean streamflow is projected to decrease by 61.91–112.16 m^3/s on average, corresponding to a decrease of 14.08–25.51% from the baseline.

Overall, our study provides a preliminary assessment of future streamflow trends in the data-scarce and hydrologically complex MRB under the combined pressures of climate change and intensive human activities. Our findings offer a scientific basis for informing adaptive water management strategies in the MRB.

Author Contributions: M.C.: Conceptualization, Methodology, Software, Formal Analysis, Data Curation, Writing—Original Draft, Writing—Review and Editing, Project Administration, and Funding Acquisition; K.C.: Methodology; T.W.: Methodology and Writing—Review and Editing; C.L.: Writing—Original Draft. All authors have read and agreed to the published version of the manuscript.

Funding: This research was supported by a project examining the coupled hydrological–hydrodynamic simulation platform for river basins in the Chengdu–Chongqing region (Grant No. KY2024-CQ-02-01) and the National Natural Science Foundation of China (Grant No. U2340208).

Data Availability Statement: No new data were created or analyzed in this study. Data sharing is not applicable to this article.

Acknowledgments: We gratefully acknowledge the financial support provided by the project examining the coupled hydrological–hydrodynamic simulation platform for river basins in the Chengdu–Chongqing region and the National Natural Science Foundation of China.

Conflicts of Interest: Minghao Chen and Kaijie Chen are employed by the PowerChina Huadong Engineering Corporation Limited and PowerChina Chongqing Engineering Corporation Limited. The remaining authors declare that the research was conducted in the absence of any commercial or financial relationships that could be construed as a potential conflict of interest.

References

1. Chishtie, F.A.; Ali, R.U.; Bahremand, A.; Hassan, M.; Clague, J.J. Distribution-informed machine learning for flash flood susceptibility: Integrating Weibull extreme value theory with interpretable models. *Sci. Rep.* **2026**, *16*, 21652. [CrossRef]
2. Clarke, B.; Barnes, C.; Rodrigues, R.; Zachariah, M.; Alves, L.M.; Haarsma, R.; Pinto, I.; Yang, W.; Vahlberg, M.; Vecchi, G.; et al. Climate change and El Niño behind extreme precipitation leading to major floods in southern Brazil in 2024. *npj Nat. Hazards* **2026**, *3*, 4. [CrossRef]
3. Tonkin, J.D.; Siqueira, T.; Merder, J.; Datry, T.; Poff, N.L.; Talbot-Jones, J.; Olden, J.D. Extreme events and river biodiversity under climate change. *Nat. Rev. Biodivers.* **2026**, *2*, 150–169. [CrossRef]

4. Vegad, U.; Mishra, V. Climate change and effectiveness of dams in flood mitigation in India. *npj Nat. Hazards* **2025**, *2*, 63. [CrossRef]
5. Ma, H.; Nittrouer, J.A.; Fu, X.; Parker, G.; Zhang, Y.; Wang, Y.; Wang, Y.; Lamb, M.P.; Cisneros, J.; Best, J.; et al. Amplification of downstream flood stage due to damming of fine-grained rivers. *Nat. Commun.* **2022**, *13*, 3054. [CrossRef] [PubMed]
6. Nguyen, L.; Todorovic, L.; Ombadi, M. Anthropogenic global warming increases the risk of record-breaking extreme precipitation events in low-income countries. *Commun. Earth Environ.* **2026**, *7*, 646. [CrossRef]
7. Liao, N.; Zhang, L.; Chen, M.; Li, J.; Wang, H. The influence mechanism of water level operation on algal blooms in canyon reservoirs and bloom prevention. *Sci. Total Environ.* **2024**, *912*, 169377. [CrossRef] [PubMed]
8. Tang, W. Research on Optimal Scheduling of Zipingpu Reservoir Based on Downstream Ecological Environment Demand. Master's Thesis, Sichuan University, Chengdu, China, 2023. (In Chinese) [CrossRef]
9. Yang, L.; You, L.H. Multi-objective dispatching operation practice of Zipingpu Reservoir during flood season. *Sichuan Hydro Power* **2018**, *37*, 24–26, 30. (In Chinese) [CrossRef]
10. Chen, M.; Li, C.; Hu, Z.; Wang, T.; Tang, L.; Yang, D. Shifting water and energy controls on hydrological processes under climate change in the topographically complex Min–Tuo River Basin, southwest China. *J. Hydrol. Reg. Stud.* **2026**, *65*, 103352. [CrossRef]
11. Hou, J.; Ye, A.; You, J.; Ma, F.; Duan, Q. An estimate of human and natural contributions to changes in water resources in the upper reaches of the Minjiang River. *Sci. Total Environ.* **2018**, *635*, 901–912. [CrossRef] [PubMed]
12. Zhang, Y.; Ye, A.; You, J.; Jing, X. Quantification of human and climate contributions to multi-dimensional hydrological alterations: A case study in the Upper Minjiang River, China. *J. Geogr. Sci.* **2021**, *31*, 1102–1122. [CrossRef]
13. Wang, T.; Shi, R.; Yang, D.; Yang, S.; Fang, B. Future changes in annual runoff and hydroclimatic extremes in the upper Yangtze River Basin. *J. Hydrol.* **2022**, *615*, 128738. [CrossRef]
14. Wang, Y.; Ni, F.; Deng, Y.; Zhu, M.; Wen, W.; Wu, M.; Ren, H. Spatio-temporal dynamics of blue-green water resources in the Min-Tuo River Basin: A coupled SWAT-FLUS-CMIP6 modeling approach. *J. Hydrol.* **2026**, *674*. [CrossRef]
15. Jiang, N.; Ni, F.; Deng, Y.; Wu, M.; Yue, Z.; Zhu, M.; Ren, H.; Wang, Y. The impact of future climate and land use changes on runoff in the Min-Tuo River Basin. *J. Water Clim. Change* **2024**, *15*, 5518–5539. [CrossRef]
16. Yang, K.; Chen, T.; Ao, T.; Zhang, X.; Zhou, L.; Gao, D. Response of runoff in the upper reaches of the Minjiang River to climate change. *J. Water Clim. Change* **2022**, *13*, 260–273. [CrossRef]
17. Liu, C.; Liu, J.; Zhang, L.; Shrestha, U.B.; Luo, D.; Wei, Y.; Wang, J. Assessing climate and land use change impacts on ecosystem services in the upper Minjiang River Basin. *Remote Sens.* **2025**, *17*, 1884. [CrossRef]
18. Liang, S.; Wang, W.; Zhang, D.; Li, Y.; Wang, G. Quantifying the im-pacts of climate change and human activities on runoff variation: Case study of the upstream of Minjiang River, China. *J. Hydrol. Eng.* **2020**, *25*, 05020026. [CrossRef]
19. Xu, J.; Lv, C.; Yao, L.; Hou, S. Intergenerational equity based optimal water allocation for sustainable development: A case study on the upper reaches of Minjiang River, China. *J. Hydrol.* **2019**, *568*, 492–504. [CrossRef]
20. Yang, D.; Herath, S.; Musiake, K. Development of a geomorphology-based hydrological model for large catchments. *Proc. Hydraul. Eng.* **1998**, *42*, 169–174. [CrossRef]
21. Yang, D.W.; Gao, B.; Jiao, Y.; Lei, H.M.; Zhang, Y.L.; Yang, H.B.; Cong, Z.T. A distributed scheme developed for eco-hydrological modeling in the upper Heihe River. *Sci. China Earth Sci.* **2015**, *58*, 36–45. [CrossRef]
22. Zhai, H.; Wang, M.; Shen, D.; Hu, B.; Li, Y. Analysis of runoff variation and driving factors in the Minjiang River Basin over the last 60 years. *J. Water Clim. Change* **2022**, *13*, 3675–3691. [CrossRef]
23. Chen, M.; Li, C.; Wang, T. A novel data-driven attribution analysis of long-term streamflow changes in the heavily regulated, data-scarce middle reach of the Minjiang River. *Hydrology* **2026**, *13*, 172. [CrossRef]
24. New, M.; Hulme, M.; Jones, P. Representing twentieth-century space–time climate variability. Part II: Development of 1901–96 monthly grids of terrestrial surface climate. *J. Clim.* **2000**, *13*, 2217–2238. [CrossRef]
25. Shen, Y.; Xiong, A.Y. Validation and comparison of a new gauge-based precipitation analysis over mainland China. *Int. J. Climatol.* **2016**, *36*, 252–265. [CrossRef]
26. Jarvis, A.; Guevara, E.; Reuter, H.I.; Nelson, A. *Hole-Filled SRTM for the Globe: Version 4: Data Grid*; CGIAR-CSI: Montpellier, France, 2008.
27. Cao, S.; Li, M.; Zhu, Z.; Wang, Z.; Zha, J.; Zhao, W.; Duanmu, Z.; Chen, J.; Zheng, Y.; Chen, Y.; et al. Spatiotemporally consistent global dataset of the GIMMS leaf area index (GIMMS LAI4g) from 1982 to 2020. *Earth Syst. Sci. Data* **2023**, *15*, 4877–4899. [CrossRef]
28. FAO; IIASA; ISRIC; ISS-CAS; JRC. *Harmonized World Soil Database*, version 1.2; FAO: Rome, Italy; IIASA: Laxenburg, Austria, 2012.
29. Dai, Y.J.; Shangguan, W.; Duan, Q.Y.; Liu, B.Y.; Fu, S.H.; Niu, G. Development of a China dataset of soil hydraulic parameters using pedotransfer functions for land surface modeling. *J. Hydrometeorol.* **2013**, *14*, 869–887. [CrossRef]
30. Eyring, V.; Bony, S.; Meehl, G.A.; Senior, C.A.; Stevens, B.; Stouffer, R.J.; Taylor, K.E. Overview of the Coupled Model Intercomparison Project Phase 6 (CMIP6) experimental design and organization. *Geosci. Model Dev.* **2016**, *9*, 1937–1958. [CrossRef]

31. Gidden, M.J.; Riahi, K.; Smith, S.J.; Fujimori, S.; Luderer, G.; Kriegler, E.; van Vuuren, D.P.; Berg, M.v.D.; Feng, L.; Klein, D.; et al. Global emissions pathways under different socioeconomic scenarios for use in CMIP6: A dataset of harmonized emissions trajectories through the end of the century. *Geosci. Model Dev.* **2019**, *12*, 1443–1475. [CrossRef]
32. Jiang, D.; Hu, D.; Tian, Z.; Lang, X. Differences between CMIP6 and CMIP5 models in simulating climate over China and the East Asian monsoon. *Adv. Atmos. Sci.* **2020**, *37*, 1102–1118. [CrossRef]
33. Li, Y.; Yan, D.; Peng, H.; Xiao, S. Evaluation of precipitation in CMIP6 over the Yangtze River Basin. *Atmos. Res.* **2021**, *253*, 105406. [CrossRef]
34. Wang, Y.; Yang, H.; Gao, B.; Wang, T.; Qin, Y.; Yang, D. Frozen ground degradation may reduce future runoff in the headwaters of an inland riv-er on the northeastern Tibetan Plateau. *J. Hydrol.* **2018**, *564*, 1043–1057. [CrossRef]
35. Gao, B.; Yang, D.W.; Qin, Y.; Wang, Y.H.; Li, H.Y.; Zhang, Y.L.; Zhang, T.J. Change in frozen soils and its effect on regional hydrology, upper Heihe basin, northeastern Qinghai-Tibetan Plateau. *Cryosphere* **2018**, *12*, 657–673. [CrossRef]
36. Yang, L.; Zeng, S.; Xia, J.; Wang, Y.; Huang, R.; Chen, M. Effects of the Three Gorges Dam on the downstream streamflow based on a large-scale hydrological and hydrodynamics coupled model. *J. Hydrol. Reg. Stud.* **2022**, *40*, 101039. [CrossRef]
37. Flerchinger, G.; Saxton, K. Simultaneous heat and water model of a freezing snow-residue-soil system I. Theory and development. *Trans. ASAE* **1989**, *32*, 565–571. [CrossRef]
38. Yang, D.; Herath, S.; Musiake, K. A hillslope-based hydrological model using catchment area and width functions. *Hydrol. Sci. J.* **2002**, *47*, 49–65. [CrossRef]
39. Van Genuchten, M.T. A closed-form equation for predicting the hydraulic conductivity of unsaturated soils. *Soil Sci. Soc. Am. J.* **1980**, *44*, 892–898. [CrossRef]
40. Qin, Y.; Yang, D.W.; Gao, B.; Wang, T.H.; Chen, J.S.; Chen, Y.; Wang, Y.H.; Zheng, G.H. Impacts of climate warming on the frozen ground and eco-hydrology in the Yellow River source region, China. *Sci. Total Environ.* **2017**, *605*, 830–841. [CrossRef] [PubMed]
41. Hansson, K.; Simunek, J.; Mizoguchi, M.; Lundin, L.C.; van Genuchten, M.T. Water flow and heat transport in frozen soil: Numerical solution and freeze-thaw applications. *Vadose Zone J.* **2004**, *3*, 693–704. [CrossRef]
42. Farquhar, G.D.; Caemmerer, S.V.; Berry, J.A. A biochemical model of photosynthetic CO_2 assimilation in leaves of C_3 species. *Planta* **1980**, *149*, 78–90. [CrossRef] [PubMed]
43. Chen, T.; Guestrin, C. XGBoost: A scalable tree boosting system. *arXiv* **2016**, arXiv:1603.02754. [CrossRef]
44. Sun, S.; Chen, H.; Sun, G.; Ju, W.; Wang, G.; Li, X.; Yan, G.; Gao, C.; Huang, J.; Zhang, F.; et al. Attributing the changes in reference evapotranspiration in Southwestern China using a new separation method. *J. Hydrometeorol.* **2017**, *18*, 777–798. [CrossRef]
45. Liu, L.; Ao, T.; Zhou, L.; Takeuchi, K.; Gusyev, M.; Zhang, X.; Wang, W.; Ren, Y. Comprehensive evaluation of parameter importance and optimization based on the integrated sensitivity analysis system: A case study of the BTOP model in the upper Min River Basin, China. *J. Hydrol.* **2022**, *610*, 127819. [CrossRef]
46. Li, H.; Yang, D.; Zhu, Z.; Wei, Y.; Zhou, Y.; Ishidaira, H.; Commey, N.A.; Cheng, H. Flood risk analysis of urban agglomerations in the Yangtze River Basin under extreme precipitation based on remote sensing technology. *Remote Sens.* **2024**, *16*, 4289. [CrossRef]

Disclaimer/Publisher's Note: The statements, opinions and data contained in all publications are solely those of the individual author(s) and contributor(s) and not of MDPI and/or the editor(s). MDPI and/or the editor(s) disclaim responsibility for any injury to people or property resulting from any ideas, methods, instructions or products referred to in the content.